GEOPHYSICS, VOL. 86, NO. 2 (MARCH-APRIL 2021); P. EN39–EN50, 13 FIGS.
10.1190/GEO2020-0096.1

Check for updates

Downloaded 02/18/21 to 194.254.220.11. Redistribution subject to SEG license or copyright; see Terms of Use at https://library.seg.org/page/policies/terms
DOI:10.1190/geo2020-0096.1

Multiwindow weighted stacking of surface-wave dispersion

Sylvain Pasquet[1], Wei Wang[2], Po Chen[2], and Brady A. Flinchum[3]

ABSTRACT

Surface-wave methods are classically used to characterize shear (S-) wave velocities (V_S) of the shallow subsurface through the inversion of dispersion curves. When targeting 2D shallow structures with sharp lateral heterogeneity, windowing and stacking techniques can be implemented to provide a better description of V_S lateral variations. These techniques, however, suffer from the trade-off between lateral resolution and depth of investigation (DOI), which is well-known when using the multichannel analysis of surface waves (MASW) method. We have adopted a novel methodology aimed at enhancing lateral resolution and DOI of MASW results through the use of multiwindow weighted stacking of surface waves (MW-WSSW). MW-WSSW consists of stacking dispersion images obtained from data segments of different sizes, with a wavelength-based weight that depends on the aperture of the data selection window. In that sense, MW-WSSW provides additional weight to short wavelengths in smaller windows so as to better inform shallow parts of the subsurface, and vice versa for deeper velocities. Using multiple windows improves the DOI, whereas applying wavelength-based weights enhances the shallow lateral resolution. MW-WSSW was implemented within the open-source package SWIP and applied to the processing of synthetic and real data sets. In both cases, we compared it with standard windowing and stacking procedures that are already implemented in SWIP. MW-WSSW provided convincing results with optimized lateral extent, improved shallow resolution, and increased DOI.

INTRODUCTION

Surface-wave (SW) methods are classically used to characterize the mechanical properties of the shallow subsurface through the indirect estimation of shear (S-) wave velocities (V_S) (Socco and Strobbia, 2004; Socco et al., 2010). These methods are commonly used for a wide range of applications such as subsurface water content quantification (Pasquet et al., 2016a, 2016b; Lu et al., 2019), geotechnical studies (Cardarelli et al., 2014; Pegah and Liu, 2016; Jaganathan, 2019), landslide characterization (Petronio et al., 2016), hydrologic monitoring (Pasquet et al., 2015a; Bergamo et al., 2016; Dangeard et al., 2018), and archaeological investigations (Di Fiore et al., 2016). Although there is a growing interest in passive SW studies to target near-surface features (Cheng et al., 2019; Keifer et al., 2019; Wang et al., 2019a), active seismic methods are still predominantly used for such shallow applications. Active seismic data are usually acquired following a standard procedure that consists of recording the propagation of elastic waves generated by an artificial source with a linear array of geophones. The seismic signal contained in these recordings is dominated by SW (Rayleigh or Love), which are dispersive by nature and are thus sensitive to distinct portions of the subsurface at different frequencies. Because SW propagation is mostly controlled by subsurface shear properties, it is possible to link the phase velocity of SW at given frequencies to variations of V_S with depth (Gabriels et al., 1987).

Although full-waveform inversion of the seismic signal has recently shown promising results (Groos et al., 2017; Khosro Anjom et al., 2019; Pan et al., 2019), it is still computationally consuming and usually requires considerable a priori information. In this context, the multichannel analysis of surface waves (MASW) (Park et al., 1999) method remains the most common approach to estimate subsurface V_S from SW dispersion. It is mostly applied to the vertical component of Rayleigh waves, but it also can be used to retrieve V_S from their horizontal component (Ikeda et al., 2015) or

Manuscript received by the Editor 26 February 2020; revised manuscript received 23 September 2020; published ahead of production 12 December 2020; published online 11 February 2021.
[1]Université de Paris, Institut de physique du globe de Paris, CNRS, Paris F-75005, France. E-mail: pasquet@ipgp.fr (corresponding author).
[2]University of Wyoming, Department of Geology and Geophysics, Laramie, Wyoming 82071, USA. E-mail: wangxiawei0619@gmail.com; pchen@uwyo.edu.
[3]Clemson University, Environmental Engineering and Earth Sciences Department, Clemson, South Carolina 29625, USA. E-mail: bflinch@clemson.edu.
© 2021 Society of Exploration Geophysicists. All rights reserved.

Downloaded 02/18/21 to 194.254.220.11. Redistribution subject to SEG license or copyright; see Terms of Use at https://library.seg.org/page/policies/terms
DOI:10.1190/geo2020-0096.1

from Love waves (Xia et al., 2012; Mi et al., 2018, 2020). MASW relies on the transformation of seismic data collected in the space-time (x-t) domain from an array of geophones into the frequency-wavenumber (f-k) or frequency-phase velocity (f-v) domain. Several techniques exist to compute these dispersion images such as the f-k transform (Gabriels et al., 1987; Serdyukov et al., 2018), τ-p transform (McMechan and Yedlin, 1981), p-ω transform (Russel, 1987; Mokhtar et al., 1988), and multioffset phase analysis (Strobbia and Foti, 2006). All of these techniques basically convert the wavefield recorded along a 2D array into a dispersion image that describes an average 1D model of the subsurface under the array. The dispersion image is characterized by coherent maxima that correspond to SW propagation modes and that can be picked to build dispersion curves (phase velocity versus frequency relationships). Several forward modeling techniques (Thomson, 1950; Haskell, 1953; Dunkin, 1965; Kennett, 1974; Naskar and Kumar, 2019) have been developed to quickly compute synthetic dispersion curves in layered media. These forward models are commonly implemented for MASW in various linearized (Lai et al., 2002; O'Neill et al., 2003; Herrmann, 2013) or Monte Carlo (Socco and Boiero, 2008; Wathelet, 2008) inversion schemes aimed at reconstructing 1D V_S models.

When targeting 2D shallow structures with sharp lateral heterogeneity, O'Neill et al. (2003) propose to split the seismic records into multiple segments representative of successive 1D portions of the subsurface. Such a windowing procedure generates a set of dispersion images that provides a better description of the near-surface lateral variations. Using a short window effectively produces dispersion images that are more representative of the medium in the direct surroundings of the selected segment. Conversely, it also deteriorates the spectral resolution of dispersion images, thus preventing the accurate identification of phase velocities at a low frequency (i.e., at large wavelengths). This trade-off between lateral resolution and depth of investigation (DOI) is well-known in the SW community (Forbriger, 2003; Bodet et al., 2005; Mi et al., 2017). It has been tackled by numerous authors in the past two decades, either by implementing refined windowing strategies (Bohlen et al., 2004; Boiero and Socco, 2011; Bergamo et al., 2012; Ikeda et al., 2013; Onnis et al., 2019), constructing composite dispersion curves (Olafsdottir et al., 2018), or by stacking dispersion images computed from multiple sources at coinciding segments (Grandjean and Bitri, 2006; Neducza, 2007). These techniques are mostly aimed at (1) limiting the lateral footprint of dispersion measurements to better describe local variations of V_S and (2) increasing the signal-to-noise ratio (S/N) so as to help the identification of dispersion curves (especially at a low frequency) and extend the DOI.

Building on this common effort, Pasquet and Bodet (2017) present an open-source code (surface-wave dispersion inversion and profiling [SWIP]) combining windowing and stacking techniques, aim at reconstructing 1D to 2D variations of V_S from all kinds of linear active-source, near-surface seismic data. They introduce the possibility of stacking dispersion images obtained from multiple windows with different apertures, but they do not further discuss the potential benefits of such an approach. Here, we propose to take advantage of this stacking strategy to improve the lateral resolution and DOI of MASW results. We particularly developed a novel procedure for the stacking of surface waves (SSW) using wavelength-based weights to more reliably inform V_S models. The multiwindow weighted stacking of surface waves (MW-WSSW) method relies on the overarching idea that seismic data segments of different sizes better describe different portions of the subsurface. Small windows, for instance, contain crucial information about small-scale, shallow velocities, whereas wider windows incorporate deeper and larger scale features. Instead of uniformly stacking dispersion images, MW-WSSW therefore applies more weight to short wavelengths in smaller windows to better inform shallow parts of the subsurface, and vice versa for large wavelengths in wider windows.

In the following, we first provide a quick summary of the SWIP workflow. We then describe the MW-WSSW method and how it is implemented in SWIP. We finally apply MW-WSSW to synthetic and real data cases, and we compare it with standard windowing and stacking procedures.

METHOD

We start by summarizing the processing workflow implemented in SWIP and give specific emphasis on the data windowing and dispersion stacking methodology. We refer readers to Pasquet and Bodet (2017) for more details about SWIP's theoretical background. We then introduce the newly developed MW-WSSW procedure and some associated improvements of SWIP, all aimed at enhancing the lateral resolution and the DOI of V_S models obtained by MASW.

General workflow

SWIP has been designed to make the most of near-surface linear seismic records and image V_S 2D lateral variations. The first step of the implemented workflow consists of windowing the seismic data in the space-time domain so as to reduce the lateral footprint of surface-wave dispersion below each data subset, and thus allow for a 1D representation of the subsurface (O'Neill et al., 2003; Grandjean and Bitri, 2006). The selected subsets are then transformed in the frequency-phase velocity domain (dispersion image) with a p-ω slant stack (Russel, 1987; Mokhtar et al., 1988) and are subsequently summed up together at each position (Neducza, 2007) so as to improve the S/N, minimize near-field effects, and grant access to larger wavelengths and thus expand the DOI (Forbriger, 2003). Dispersion curves (i.e., phase-velocity versus frequency relationships) are then picked for each stacked dispersion image with the phase-velocity errors estimated through the algorithm proposed by O'Neill (2003). The picked dispersion curves are inverted independently with the neighborhood algorithm (NA) (Sambridge, 1999; Wathelet et al., 2004), in which forward modeling is performed using the Thomson-Haskell matrix propagator technique (Thomson, 1950; Haskell, 1953) as implemented by Dunkin (1965). The inversion finally provides a set of consecutive 1D V_S models that are eventually combined to build a 2D section (Pasquet et al., 2015b) depicting the variations of V_S laterally and at depth.

Data windowing and dispersion stacking

More specifically, SWIP takes advantage of typical multishot acquisition setups to recover lateral variations of SW dispersion using shot gather windowing and dispersion stacking (O'Neill et al., 2003; Grandjean and Bitri, 2006; Neducza, 2007). These techniques extract spatial subsets of the seismic data in which the subsurface

Downloaded 02/18/21 to 194.254.220.11. Redistribution subject to SEG license or copyright; see Terms of Use at https://library.seg.org/page/policies/terms
DOI:10.1190/geo2020-0096.1

medium can realistically be considered 1D. In SWIP, these techniques are implemented as follows (Figure 1):

1) Select subsets of seismic data centered around a specific midpoint (X_{mid}) from a set of N spatial windows with varying apertures (A_n).
2) Identify all shots located within dS_{min} and dS_{max} traces from each data subset.
3) Extract data subsets for each selected pair of shot and window.
4) Transform the wavefield of extracted data subsets into the frequency-phase velocity domain (dispersion image) with a slant stack (Russel, 1987; Mokhtar et al., 1988).
5) Normalize the amplitude spectrum of all dispersion images.
6) Stack the normalized dispersion images computed for the current X_{mid}.
7) Shift the midpoint by dW traces and repeat steps 1–6 at the following X_{mid}.

The original windowing and stacking techniques proposed by O'Neill et al. (2003), Grandjean and Bitri (2006), or Neducza (2007) usually consist of computing dispersion images with a single window width and stacking them together to enhance the S/N. The aperture of the window is thus a critical parameter that needs to be picked with care because it will define the lateral resolution and DOI. Increasing the window aperture expands the DOI while severely decreasing the lateral resolution, especially in the presence of sharp lateral heterogeneities. However, using smaller windows provides high-resolution characterization of these lateral changes, although drastically reducing the depth of penetration. To overcome this inherent trade-off, Pasquet and Bodet (2017) introduce stacking of dispersion images obtained from windows with different apertures and centered at a common X_{mid} position. Such a stacking procedure is aimed at improving the characterization of shallow lateral changes and deep velocities from the information contained in multiple windows with varying apertures. However, the advantages or drawbacks of using the multiwindow stacking of surface-wave (MW-SSW) method were not discussed therein and are thus the main focus of the current study.

MW-WSSW

In this paper, we propose to take advantage of such a multiwindow extraction design to enhance the lateral resolution of V_{S} models and increase their DOI. To go further, we introduce MW-WSSW, an advanced procedure that relies on wavelength-weighted stacking of dispersion images based on the aperture of the extraction window. A similar approach was used by Bohlen et al. (2004) and Bergamo et al. (2012) to extract the seismic record in the time-space domain with a set of Gaussian functions. Here, we propose to use such Gaussian functions in the frequency-phase velocity domain to weight dispersion images extracted with different apertures. This new procedure was added in the processing workflow between steps 4 and 5 from the list above. After obtaining dispersion images for the different apertures, we define a set of Gaussian functions (one per aperture) spanning the whole range of wavelengths contained in the seismic signal so as to give more weight to large wavelengths in the longer windows and vice versa. For each aperture A_n, the Gaussian weighting function w_n is defined as follows:

$$w_n = e^{-\frac{1}{2}\left(\frac{1}{a}\frac{\lambda-\lambda_c}{\sigma}\right)^2}, \tag{1}$$

where a is a parameter controlling the width of the Gaussian and λ_c is its central wavelength defined as

$$\lambda_c = 1.5 \cdot A_n, \tag{2}$$

where A_n is the window aperture, which we define as

$$A_n = A_{\mathrm{min}} : dA : A_{\mathrm{max}}. \tag{3}$$

We also define λ_n as the maximum acceptable wavelength for a given window aperture. This wavelength corresponds to the lower limit of the dispersion curves, and it is crucial in the inversion process because it controls the DOI of the V_{S} models. There is currently no unequivocal criterion to define this wavelength; some authors limit it down in frequency with an amplitude threshold (Pasquet et al., 2015a, 2015b), while others restrict it between 25% and 50% of the extraction window aperture (O'Neill, 2003; Bodet et al., 2005, 2009). Here, we define λ_n as a power law function of the window aperture A_n such that

$$\lambda_n = A_n \cdot 10^{\left(\frac{A_n}{2}\right)^{-0.5}}. \tag{4}$$

In equation 1, the width of the Gaussian is also controlled by the standard deviation σ, defined by the number of extraction windows (N) and the range of wavelengths computed with equation 4:

$$\sigma = \frac{1}{\sqrt{2\pi}}\frac{\lambda_{\mathrm{max}} - \lambda_{\mathrm{min}}}{N}. \tag{5}$$

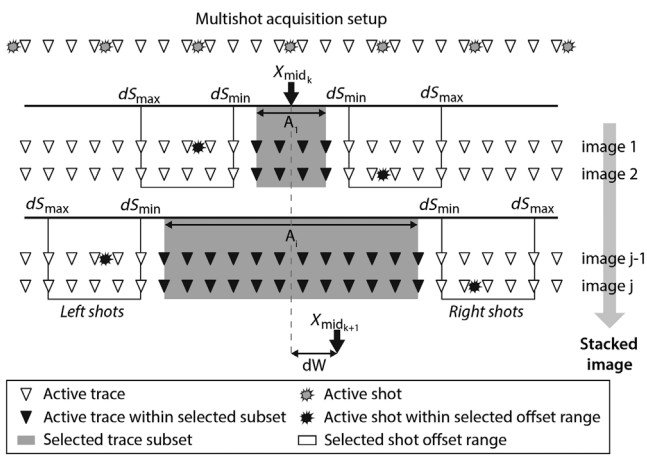

Figure 1. Workflow of seismic data windowing and dispersion stacking implemented in SWIP. Seismic data subsets are selected from a set of N spatial windows with varying apertures (A_n) centered on a specific midpoint (X_{mid}). Data subsets with shots located within dS_{min} and dS_{max} traces are extracted, with their wavefields each transformed into the frequency-phase velocity domain (dispersion image) with a slant stack. All dispersion images computed at the current X_{mid} are eventually normalized and stacked into a final image. The midpoint is finally shifted by dW traces to repeat the previous steps at the following X_{mid}. Modified after Pasquet and Bodet (2017).

Downloaded 02/18/21 to 194.254.220.11. Redistribution subject to SEG license or copyright; see Terms of Use at https://library.seg.org/page/policies/terms
DOI:10.1190/geo2020-0096.1

We eventually obtain a set of N Gaussian functions w_n (Figure 2a and 2e) spanning the whole range of acceptable wavelengths between $\lambda_{\min}$ and $\lambda_{\max}$, defined with equation 4 for smallest and largest windows. These functions are transformed into weighting matrices in the frequency-phase velocity domain with the dimensions of the computed dispersion images (Figure 2b–2d and 2f–2h). Dispersion images extracted with different apertures at a single X_{mid} position are then weighted with their associated matrix, and they are ultimately stacked together following steps 5 and 6 of the original workflow.

In the following, we test the proposed MW-WSSW procedure with different parameters and we compare it with the results of single-window and uniform (i.e., nonweighted) MW-SSW on synthetic and field data.

NUMERICAL EXAMPLES

Subsurface model and synthetic data

We first tested the MW-WSSW method on two synthetic seismic data sets simulated using (1) a simple three-layer V_S model (Figure 3a) and (2) a realistic subsurface V_S model (Figure 3c). The first model is composed of three layers with different linear dips and V_S of 250, 550, and 1200 m/s, respectively. For the second model, we used the results of a seismic refraction tomography survey performed under a granitic ridge in the Blair-Wallis watershed (Flinchum et al., 2018; Wang et al., 2019b). In both cases, we adopted the arbitrary high-order accurate derivatives discontinuous Galerkin method (Dumbser and Käser, 2006; Käser and Dumbser, 2006, 2008; Dumbser et al., 2007; Käser et al., 2007) to solve the elastic wave equation and simulate wave-propagation in a 3D mesh. We used a tetrahedral mesh with variable-size elements to fully conform to the topography of the free surface. The source-time-function was a temporal Dirac delta function band-pass filtered using a fourth-order Butterworth filter with corners at 10 and 120 Hz. Synthetic seismic data were generated so as to mimic typical acquisition arrays deployed for shallow seismic velocities characterization (Flinchum et al., 2018). We used a sampling rate of 0.125 ms and a recording time of 0.75 s, and we extracted shot gathers every 10 m along both transects, constituted of, respectively, 121 and 241 traces staggered every 1 m. Example shot gathers generated with sources located at 20 m along the three-layer model and at 40 and 120 m along the realistic model are shown Figure 3b, 3d, and 3e, respectively.

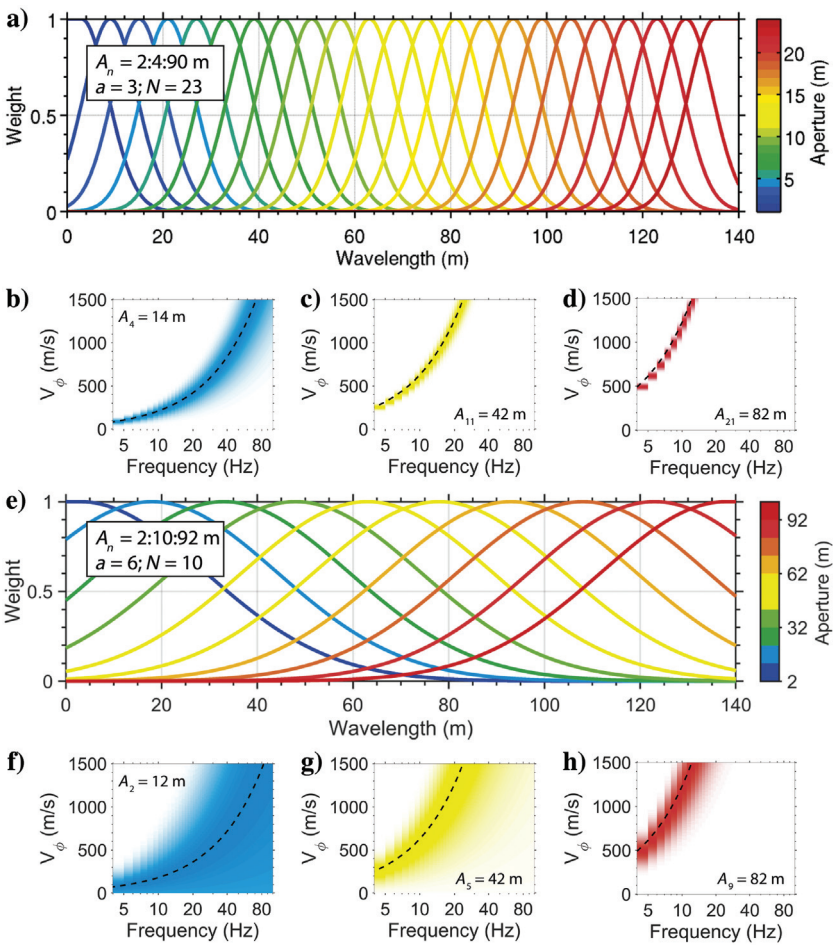

Figure 2. Example sets of Gaussian functions used to weight dispersion images prior to stacking, with (a) $A_n = 2{:}4{:}90$ m and $a = 3$ and (e) $A_n = 2{:}10{:}92$ m and $a = 6$ (equation 1). Each window is centered at a wavelength based on the aperture of the extraction window (equation 3). (b-d) and (f-h) Examples of weighting matrices for three different window apertures displayed in the frequency-phase velocity domain for both sets of Gaussian functions. Weight ranges linearly from 0 (white) to 1 (color). The black dashed lines highlight the central wavelengths of each weighting matrix.

Data processing

Three-layer model: MW-WSSW parametric study

We used the simple three-layer model to test the influence of MW-WSSW parameters on surface-wave stacking. We first investigated the influence of the width of the Gaussian function by successively changing the value of a ($a = 1$, 3, and 6), and then we examined the effect of their number with different sets of apertures ($A_n = 2{:}4{:}90$ m and $A_n = 2{:}10{:}92$ m). We also extracted dispersion images with a standard single-sized window of 23 traces ($A = 22$ m) as a means of comparison. In all cases, we used shots located between 5 ($dS_{\min}$) and 20 ($dS_{\max}$) traces away from the selected data subset and a shift of one trace ($dW = 1$) between successive windows. Coherent maxima associated with the surface waves were picked on each dispersion image and saved with their corresponding errors. These depend directly on the resolution of the dispersion images, and thus on the maximum aperture used for stacking. Examples of dispersion images computed with the different stacking procedures are shown with their associated picks and errors in Figure 4. Synthetic dispersion curves were also computed at each X_{mid} position from the true V_S model and are superimposed to dispersion images. The picked dispersion curves and the predicted data are also represented as pseudosections of phase velocity (V_ϕ) varying with λ and X_{mid} (Figure 5).

Downloaded 02/18/21 to 194.254.220.11. Redistribution subject to SEG license or copyright; see Terms of Use at https://library.seg.org/page/policies/terms
DOI:10.1190/geo2020-0096.1

For a given set of apertures A_n, using smaller a tends to generate sharp discontinuities and jumps within the dispersion image (Figure 4a), whereas using larger a produces overly smoothed images (Figure 4c). In a similar way, using fewer Gaussian functions (i.e., larger dA) (Figure 4d) can create gaps in the wavelength coverage and thus decreases the resolution at depth. In the examples shown here, and for all X_{mid} positions along the three-layer model (Figure 5), the differences between dispersion curves extracted with different a and A_n parameters are still very difficult to distinguish with the naked eye. We were eventually able to identify $a = 3$ and $A_n = 2{:}4{:}90$ m as the best set of parameters for MW-WSSW after calculating the average residuals between the picked and calculated dispersion curves (Figure 5g–5k). The comparison with standard 23-trace window results (Figure 4e) also clearly highlights how MW-WSSW enhances dispersion images at low frequencies, thus allowing deeper investigation of the subsurface.

Realistic model: Comparison with classic approaches

To test MW-WSSW in a more complex setting, we carried out surface-wave stacking on the realistic model following four different strategies using single- and multiwindow extraction schemes. In the first two cases, we stacked dispersion images from seismic data extracted with single-sized windows of 23 traces ($A = 22$ m) and 63 traces ($A = 62$ m), with shots located between 5 (dS_{min}) and 20 (dS_{max}) traces away from the selected data subset and a shift of one trace ($dW = 1$) between successive windows. With the same shot offset and window shifting parameters, we also applied uniform and weighted multiwindow stacking of dispersion images computed with 23 evenly spaced windows. Based on the parametric study performed on the three-layer model, we used $A_n = 2{:}4{:}90$ m and $a = 3$ in the MW-WSSW workflow. The same set of apertures was also used with uniform MW-SSW to compare the performance of both multiwindow approaches. We picked coherent maxima on each dispersion image and saved dispersion curves with their corresponding errors. Examples of dispersion images computed with the four stacking procedures are shown with their associated picks and errors in Figure 6. As in the three-layer case, synthetic dispersion curves were computed at each X_{mid} position from the realistic V_S model and then superimposed to dispersion images. We also represented the picked dispersion curves and the predicted data as pseudosections of phase velocity (V_ϕ) varying with λ and X_{mid} (Figure 7).

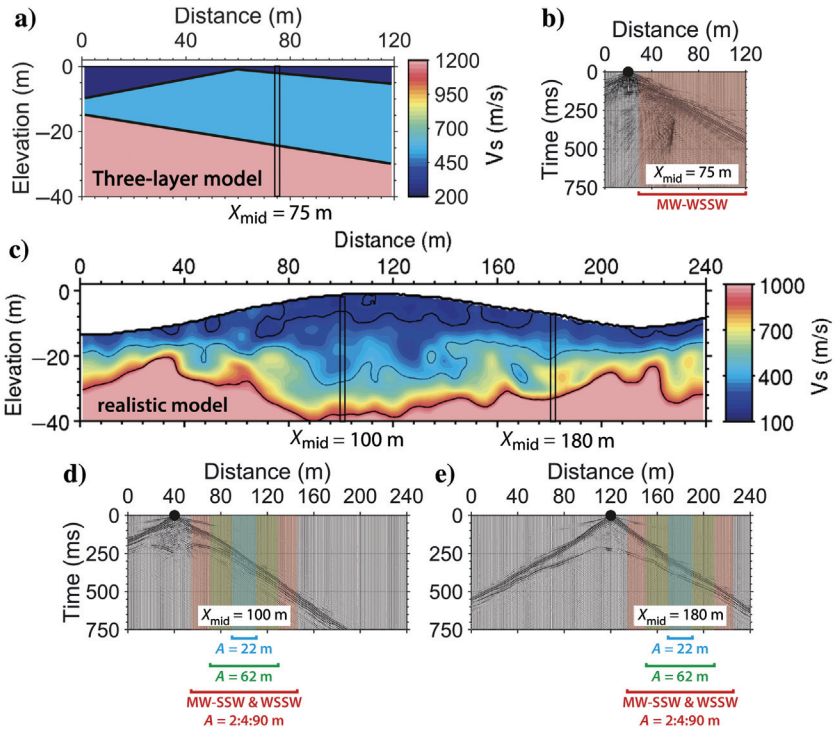

Figure 3. The V_S models used to simulate synthetic seismic data with the location of example midpoints. (a) Three-layer model with contours at 250, 550, and 1200 m/s, and midpoint at 75 m. (b) An example shot gather for the three-layer model with a source located at 20 m. (c) Realistic model with contours at 225, 450, and 900 m/s, and midpoints at 100 and 180 m. (d and e) Example shot gathers with sources located at 40 and 120 m, respectively. The apertures of different extraction windows are highlighted with the shaded areas in (b), (d), and (e).

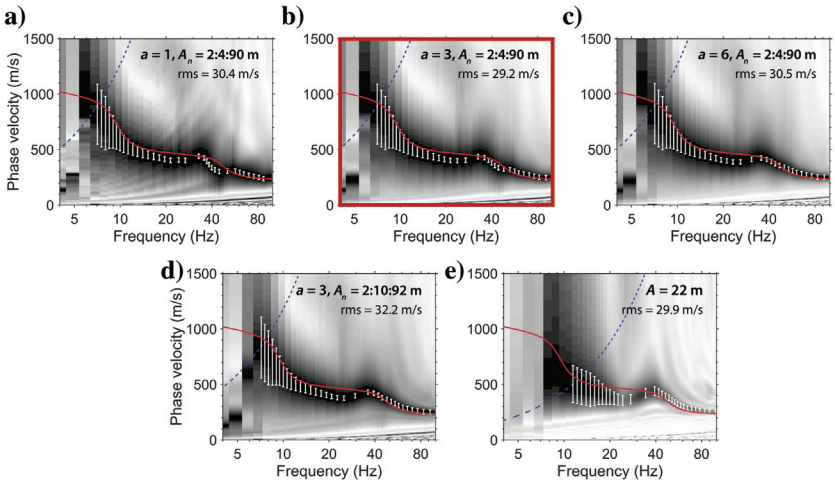

Figure 4. Examples of stacked dispersion images obtained with the three-layer model at $X_{\mathrm{mid}} = 75$ m using MW-WSSW with different sets of Gaussian functions with varying steps and widths: (a) $a = 1$ and $A_n = 2{:}4{:}90$ m, (b) $a = 3$ and $A_n = 2{:}4{:}90$ m, (c) $a = 6$ and $A_n = 2{:}4{:}90$ m, and (d) $a = 3$ and $A_n = 2{:}10{:}92$ m. (e) The dispersion image obtained with a standard single-sized window of 23 traces ($A = 22$ m). Amplitudes range linearly from 0 (white) to 1 (black). The red solid lines correspond to theoretical dispersion curves computed from the true V_S model at $X_{\mathrm{mid}} = 75$ m (Figure 3a). The blue dashed lines represent the maximum acceptable wavelengths computed with equation 4. The picked dispersion curves are shown in white with their corresponding error bars.

Downloaded 02/18/21 to 194.254.220.11. Redistribution subject to SEG license or copyright; see Terms of Use at https://library.seg.org/page/policies/terms
DOI:10.1190/geo2020-0096.1

The results obtained with the 22 m window show an overall good agreement among dispersion images maxima, picked dispersion curves, and predicted data (Figure 6a and 6b). The short aperture of the window, however, hinders the extraction of data at large wavelengths (Figure 7b), while still being too wide to capture short-wavelength features associated with shallow velocity variations depicted in the predicted phase velocity pseudosection (Figure 7a). The 62 m window allows for extracting larger wavelength information, but it complicates the identification of dispersion curves at a high frequency (Figure 6c and 6d). This leads to a deterioration of the phase velocity characterization at short wavelengths associated with a reduced lateral extent (Figure 7c). Uniform multiwindow stacking provides intermediate results with large wavelength identification associated with decent shallow characterization and complemented with an optimized lateral coverage (Figure 7d), yet dispersion curve identification can still be difficult at mid to high frequencies (Figure 6e and 6f), thus preventing the accurate estimation of shallow velocities. MW-WSSW finally turns out to be the optimal compromise because it provides (1) optimized lateral coverage, (2) accurate description of phase velocity at high frequencies, and (3) extended dispersion curves at larger wavelengths along most of the profile (Figures 6g, 6h, and 7e).

To provide a more quantitative comparison of the different windowing and stacking methods, we also show pseudosections of phase velocity residuals calculated between the picked and predicted data (Figure 8). For all four methods, the velocity residuals are between ±25%, with the optimal match and lowest standard deviation of residuals obtained with the MW-WSSW method (Figure 8d and 8h). Our new procedure gives especially good results at short wavelengths enabling high-resolution characterization of the shallow subsurface while still supplying valuable information at large wavelengths to describe the deeper horizons.

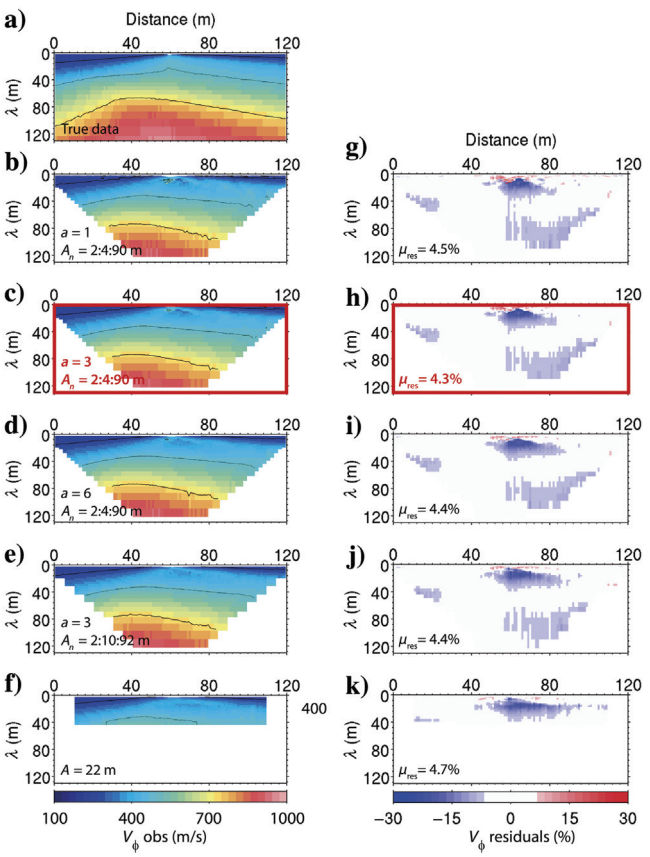

Figure 5. Pseudosections of phase velocity (V_Φ) represented as a function of wavelength and spread midpoint position with phase velocity contours at 250, 500, and 750 m/s. (a) Synthetic phase velocity data computed from the true V_S model (Figure 3a) for each spread midpoint. (b–f) Phase velocity data picked on dispersion images stacked with MW-WSSW and single-sized windowing (see Figure 4). (g–k) The corresponding phase velocity residuals.

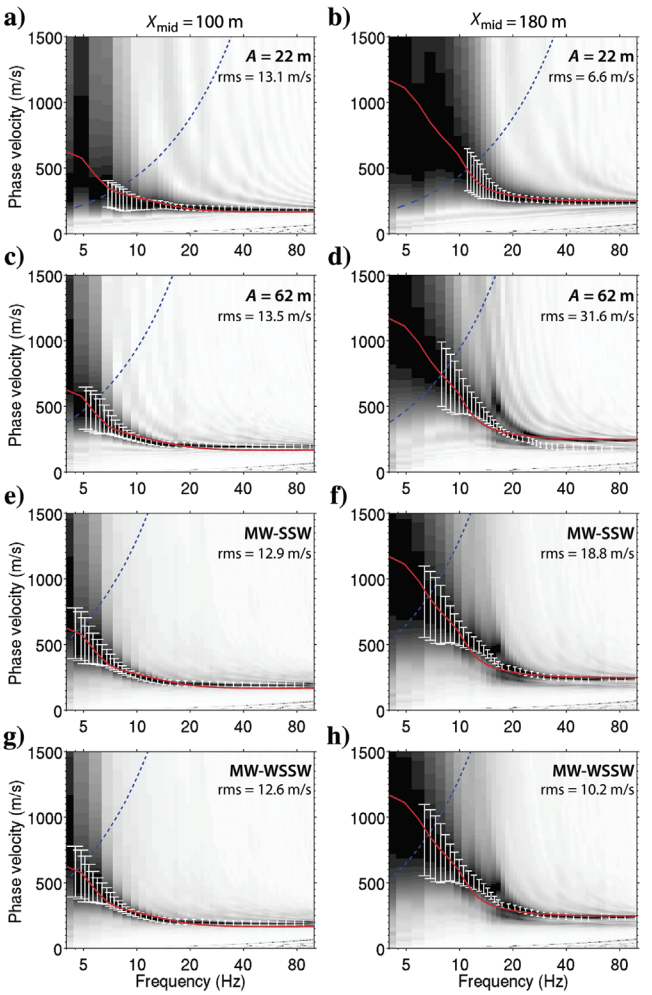

Figure 6. Examples of stacked dispersion images obtained at $X_{mid} = 100$ m (the left column) and $X_{mid} = 180$ m (the right column) using (a and b) a 22 m window, (c and d) a 62 m window, (e and f) a set of 23 windows defined as $A_n = 2{:}4{:}90$ m with uniform MW-SSW, and (g and h) a similar set of windows with MW-WSSW using $a = 3$. Amplitudes range linearly from 0 (white) to 1 (black). The red solid lines correspond to theoretical dispersion curves computed from the true V_S model at both X_{mid} positions. The blue dashed lines represent the maximum acceptable wavelengths (equation 4). The picked dispersion curves are shown in white with their corresponding error bars.

Downloaded 02/18/21 to 194.254.220.11. Redistribution subject to SEG license or copyright; see Terms of Use at https://library.seg.org/page/policies/terms
DOI:10.1190/geo2020-0096.1

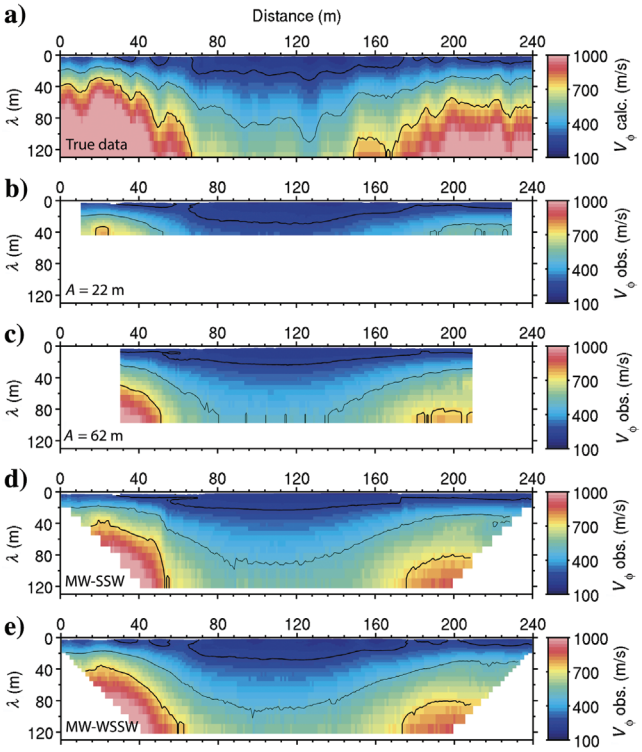

Figure 7. Pseudosections of phase velocity represented as a function of wavelength and spread midpoint position with phase velocity contours at 250, 500, and 750 m/s. (a) Synthetic phase velocity data computed from the true V_S model for each spread midpoint. Phase velocity data picked on dispersion images stacked with (b) a 22 m window, (c) a 62 m window, (d) MW-SSW, and (e) MW-WSSW.

Inversion and resulting V_S models

Three-layer model

SWIP was then used to perform successive 1D inversions of dispersion curves obtained with the two procedures giving the best results (i.e., 22 m single-window and multiwindow MW-WSSW), assuming a 1D layered medium below each extraction window. For the three-layer model, we used a parameter space with two layers overlaying the half-space, with the thickness of the first layer varying between 0.5 and 5 m and the thickness of the second layer varying between 10 and 25 m. We did not allow low-velocity zones, and we looked for V_S ranging between 10 and 2000 m/s. For each X_{mid} position, we executed a single run of NA inversions, which generated a total of 10,200 models. We then selected all models with misfits of less than 0.15 to compute an average 1D V_S model. These 1D final models were eventually merged together to build 2D sections of V_S for the selected windowing and stacking procedures (Figure 9). The final root-mean-square (rms) errors of all the models reached 11.1 m/s for the 22 m single-window model and 19.0 m/s for the MW-WSSW model.

Both methods nicely depict the shape and velocity of the upper layer. However, MW-WSSW performs better for deeper investigations, and it highlights the third layer for most parts of the profile (Figure 9c). We also computed lateral variations of the V_S residuals (Figure 9d and 9e) to provide more quantitative estimates of the model reconstruction. Except for the upper layer, the single-window procedure leads to an overall strong deviation from the true velocity model, with especially underestimated velocities at depth. However, the MW-WSSW procedure provides a model with minimized deviation, except on both sides of the model where the coverage decreases and at the center where the abrupt change of dip at the surface generates artifacts at depth.

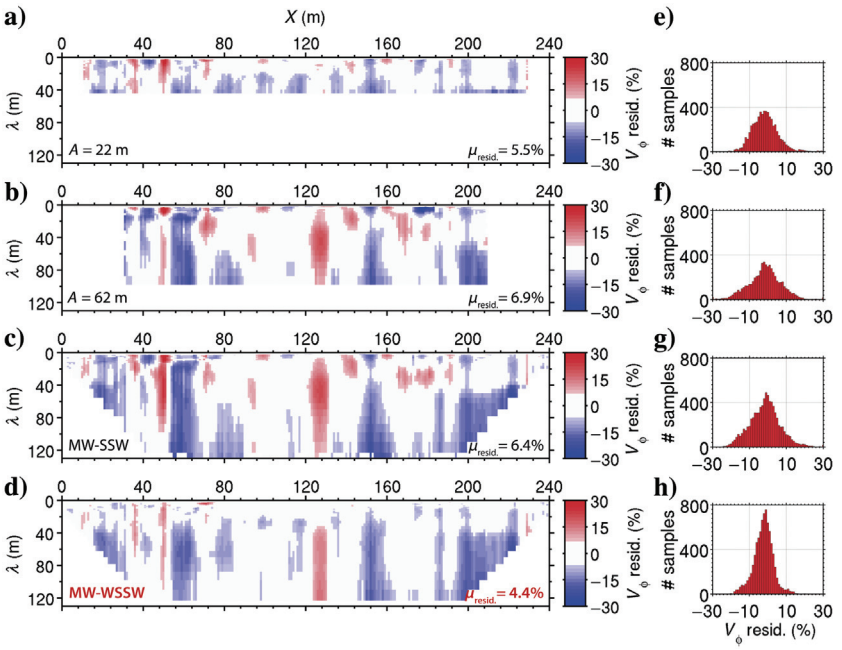

Figure 8. Pseudosections of the phase velocity residuals represented as a function of the wavelength and spread midpoint position for (a) a 22 m window, (b) a 62 m window, (c) MW-SSW, and (d) MW-WSSW. Residuals of less than 7.5% are masked. (e–h) Histograms of the phase velocity residuals.

Realistic model

In the realistic case, the parameter space was composed of 10 layers overlaying the half-space to look for smooth nonlinear velocity gradients, as expected in such a weathered granitic environment (Flinchum et al., 2018). The thickness of each layer was set to be bound between 0.5 and 1.5 m in the first layer; these limits then increased exponentially in the subsequent layers until reaching 1.5 and 6 m in the deepest layer. We looked for potential low-velocity zones by converting the variations of phase velocities (V_ϕ) versus wavelength (λ) into S-wave velocity (V_S) versus depth (d) functions using the following empirical relationships:

$$V_S \approx \frac{V_\phi}{0.95} \quad \text{and} \quad d \approx \frac{\lambda}{4}. \tag{6}$$

As a rule of thumb, the DOI is often considered to range between 1/3 and 1/2 of the maximum observed wavelength (O'Neill et al., 2003; Garofalo et al., 2016), but these criteria remain mostly empirical. After trial-and-error tests, we chose to use a more conservative factor in equation 6, that is, 1/4 of the maximum wavelength, to

Downloaded 02/18/21 to 194.254.220.11. Redistribution subject to SEG license or copyright; see Terms of Use at https://library.seg.org/page/policies/terms
DOI:10.1190/geo2020-0096.1

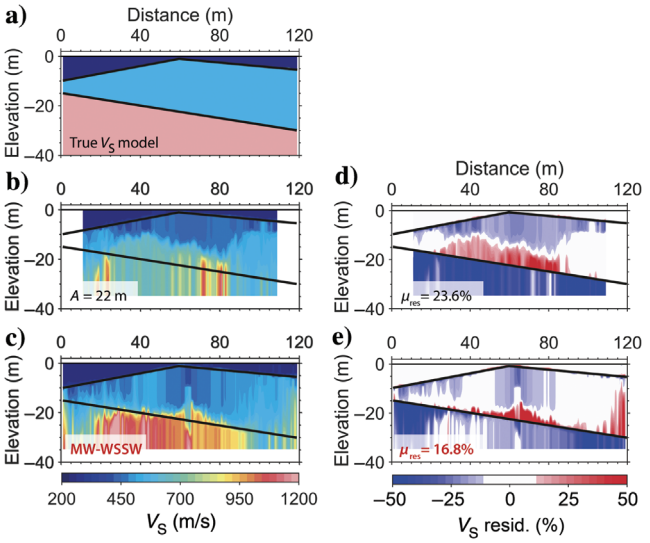

Figure 9. (a) Three-layer model used to generate synthetic data. The V_S models obtained after NA inversion using (b) a 22 m window and (c) MW-WSSW. (d and e) The corresponding V_S residuals.

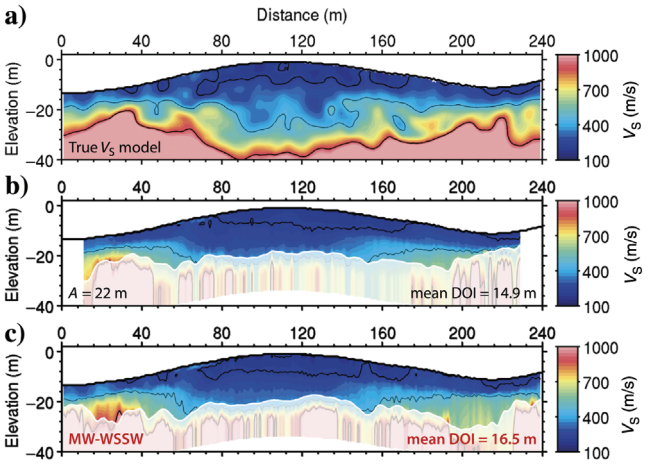

Figure 10. (a) True V_S model used to generate synthetic data. The V_S models obtained after NA inversion using (b) a 22 m window and (c) MW-WSSW. Velocity contours are shown at 225, 450, and 900 m/s. Inverted velocity models are masked below the DOI, which is defined where uncertainties are greater than 40%.

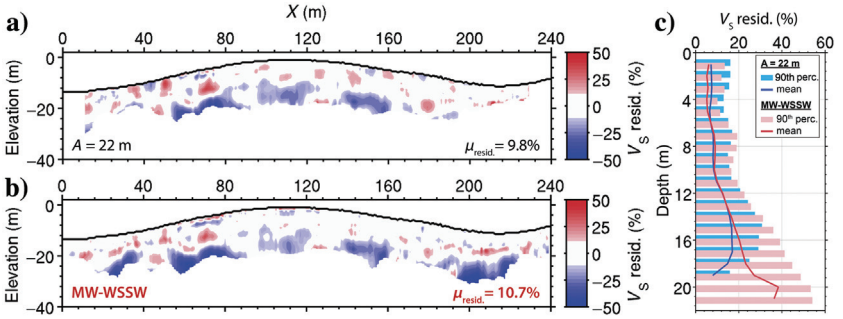

Figure 11. The V_S residuals between true model and model obtained using (a) a 22 m window and (b) MW-WSSW. Residuals of less than 12.5% are masked in (a and b). (c) Evolution of the 90th percentile and mean absolute residuals as a function of depth for both stacking procedures.

define the maximum DOI in our parameterization. We also used these empirical V_S models computed with equation 6 to constrain the evolution of V_S at depth and to reduce the computational time. Although V_S was constrained to only increase with depth by default, we authorized low-velocity zones in layers showing a reversal of empirical V_S at their corresponding average depth. In all of the layers, V_S was allowed to vary between 10 and 2500 m/s, whereas the range of V_P was defined with velocity values extracted at each X_{mid} position from the true V_P model used to simulate seismic data (not shown here) (Pasquet et al., 2015b; Pasquet and Bodet, 2017).

For each X_{mid} position, we executed two distinct runs of NA inversions, which generated a total of 50,400 models. We then selected all models matching the data within the uncertainty range and computed an average final V_S model with the associated uncertainties corresponding to the 90th percentile of all selected models. These 1D final models were eventually merged together to build 2D sections of V_S for the selected windowing and stacking procedures (Figure 10). The final rms errors of all models dropped to 6.5 m/s for the 22 m single-window model and to 10.2 m/s for the MW-WSSW model. We defined the DOI where uncertainties become higher than 40% of the estimated velocity. The mean DOI is 14.9 m for the 22 m single-window model (Figure 10b) and 16.2 m for the MW-WSSW model (Figure 10c). Both models are very similar and match closely with the true V_S model, but shallow structures (i.e., at depth < 10 m) are better defined with MW-WSSW (compare the velocity contours at 225 m/s). High-velocity structures (>1000 m/s) existing on both sides of the profile at intermediate depths are also identified with MW-WSSW while remaining mostly hidden with single-window stacking. In the central part of the profile, both methods have a similar DOI of approximately 20 m and thus fail to depict higher velocity features visible at greater depths in the realistic V_S model.

We also plotted lateral variations of the V_S residuals (Figure 11a and 11b) along with the evolution of the 90th percentile and mean absolute residuals as a function of depth (Figure 11c), which confirms the very good agreement of inverted V_S models at depths less than 12 m (mean residuals < 10% and 90% of the residuals < 20%), with a slightly better fit for MW-WSSW in the upper 5 m. Below 12 m, the 90th percentile of the residuals is mostly comprised between 20% and 40% and only exceeds 40% for samples deeper than 20 m. At these depths, MW-WSSW yields estimates of V_S that are mostly underestimated but it still provides valuable information about the main velocity trends in the subsurface.

FIELD EXAMPLE

Site description and data acquisition

We also tested the MW-WSSW method on a real seismic data set that was acquired at the hydrological observatory of Plœmeur (Brittany, France). The site is located on top of a contact between granite and micashists, separated with a subvertical fault that promotes aquifer recharge and grants favorable access to groundwater resources (Ruelleu et al., 2010). Geophysical measurements were recently carried out in Plœmeur to study the complex near-surface structure of the site and test novel acquisition and processing methodologies (Pasquet et al., 2015b; Shakas

Downloaded 02/18/21 to 194.254.220.11. Redistribution subject to SEG license or copyright; see Terms of Use at https://library.seg.org/page/policies/terms
DOI:10.1190/geo2020-0096.1

et al., 2016; Dangeard et al., 2018). In particular, Pasquet et al. (2015b) apply a single-window stacking procedure to estimate the lateral variations of V_S and compared the resulting V_S distribution with other geophysical results. Three arrays of 72 vertical 14 Hz geophones were deployed with a spacing of 4 m so as to obtain a 476 m long profile. Shots were performed between every geophone using a sledgehammer and a metal plate. For each shot, seismic data were recorded for 2 s with a 0.25 ms sampling rate.

Data processing and results

We applied the MW-WSSW procedure to process the seismic data using a set of 11 windows evenly spaced with apertures ranging from 8 to 88 m and Gaussian widths defined by $a = 3$. We kept shots located between 4 and 20 m away from each data subset, with a shift of 4 m between successive windows so as to obtain 118 stacked dispersion images regularly spaced along the profile. Dispersion curves were picked on each of them and compared with those picked in Pasquet et al. (2015b) with a 20 m window. Figure 12 especially shows the dispersion images and picks for two specific X_{mid} positions previously highlighted in Pasquet et al. (2015b). As already observed in the synthetic case, MW-WSSW allows for a better characterization of phase velocities at a low frequency, especially when the velocity gradient is sharper (Figure 12a and 12c).

We then inverted the data with SWIP using a parameterization similar to the one adopted in the synthetic realistic case. We worked with a stack of 10 layers overlaying the half-space with the minimum and maximum thicknesses of each layer increasing exponentially from 0.5 and 1.5 m, respectively, in the first layer, to 2 and 6 m in the last layer. Low-velocity zones were permitted according to the phase velocity data, following equation 6. In all layers, V_S was allowed to vary between 10 and 2500 m/s, whereas the range of V_P was defined from compressional-wave refraction tomography results obtained along the same profile (Pasquet et al., 2015b). As in the synthetic case, we performed two runs of NA inversions and generated 50,400 models. We then selected the models fitting within the uncertainty range to compute an average final V_S model with the associated uncertainties (i.e., the 90th percentile of the selected models). We merged these 1D final models into a 2D section of V_S and defined its DOI where uncertainties are greater than 40% of the estimated velocity (Figure 13). Finally, we compared the V_S model obtained from MW-WSSW with previous results of electrical resistivity and single-window SSW (Pasquet et al., 2015b). The rms errors of the single-window and MW-WSSW models were 14.3 and 14.2 m/s, respectively.

The implementation of MW-WSSW on the Plœmeur data set allowed us to increase the length of the V_S profile by approximately 80 m and the average DOI by approximately 3 m (Figure 13b and 13c). MW-WSSW also generated a model with an enhanced resolution that is more suited to characterize fine lateral variations of V_S. The MW-WSSW model remains consistent with previous results obtained at the site, and it especially shows a good agreement with the electrical resistivity model (Figure 13a). Specific features and structures, such as outcropping granite, fault zone, or clay infill overlaying micashists (Pasquet et al., 2015b), are more clearly and unequivocally defined thanks to MW-WSSW.

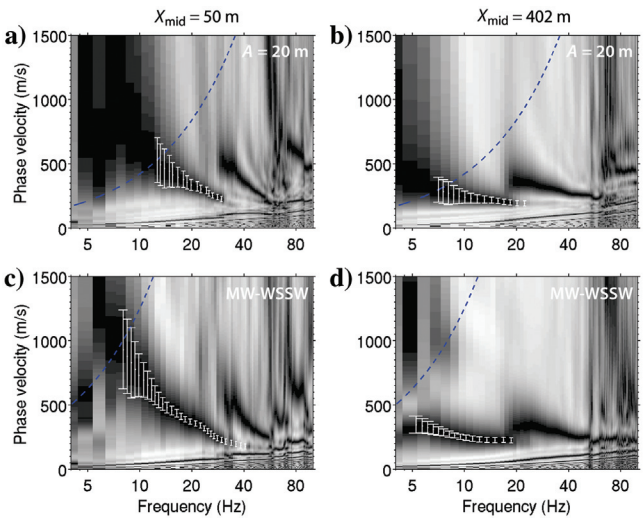

Figure 12. Examples of stacked dispersion images obtained in Plœmeur at $X_{mid} = 50$ m (the left column) and $X_{mid} = 402$ m (the right column) using (a and b) a 20 m window (after Pasquet et al., 2015b) and (c and d) MW-WSSW (this study). Amplitudes range linearly from 0 (white) to 1 (black). The blue dashed lines represent the maximum acceptable wavelengths computed with equation 4. The picked dispersion curves are shown in white with their corresponding error bars.

DISCUSSION

Applications of MW-WSSW presented in the previous sections provided satisfactory results in the synthetic and real cases. Using multiple windows of different apertures to extract surface-wave dispersion images significantly improved the reconstruction of dispersion curves at large wavelengths. Stacking these images with a wavelength-based weight helped to better resolve shallow subsurface features, which would otherwise be lost without weighting. The overall MW-WSSW procedure provided better results, in lateral resolution and DOI, than standard single-window stacking and

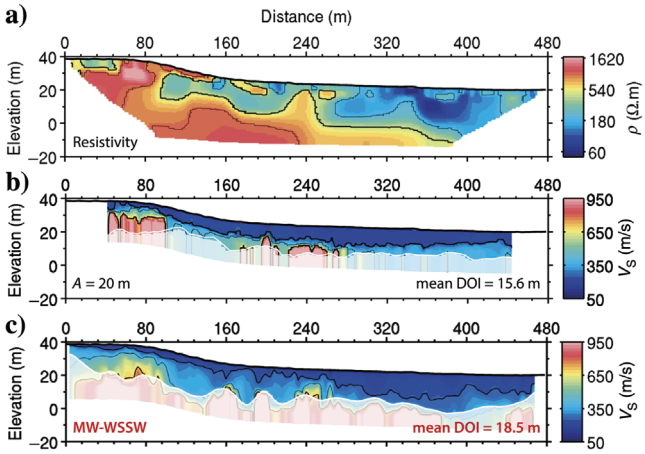

Figure 13. Geophysical profiles obtained in Plœmeur. (a) Electrical resistivity (ρ) model with contours at 200, 450, and 900 Ω.m (after Pasquet et al., 2015b). (b) The V_S model obtained with a 20 m window (after Pasquet et al., 2015b). (c) The V_S model obtained with MW-WSSW (this study). Inverted V_S models are masked below a DOI defined where uncertainties are greater than 40%. Contour lines of V_S are drawn at 250, 400, and 700 m/s in (b and c).

Downloaded 02/18/21 to 194.254.220.11. Redistribution subject to SEG license or copyright; see Terms of Use at https://library.seg.org/page/policies/terms
DOI:10.1190/geo2020-0096.1

uniform MW-SSW. The number of windows used in MW-WSSW and their respective apertures appear to be key parameters because they will control the lateral resolution. It is important to use a large number of windows that span the whole range of wavelengths to correctly describe the subtle lateral variations of velocity. Obviously, using too many windows will also drastically increase the computational time because a very large number of dispersion images will be computed and stacked for each spread midpoint position. Nonetheless, the parametric study performed on a simple three-layer model shows that the best results are obtained using the smallest possible spacing between subsequent windows ($dA = 2$ m), even though it more than doubles computational time (5+ hours with 23 windows using a 2.7 GHz six-core CPU processor versus 2 h with 10 windows in the realistic model case). One could argue that using half or one-third of the windows would still provide reasonably good results with significantly reduced computation time.

Our results illustrate the benefits of using MW-WSSW to reconstruct shallow velocity lateral variations (e.g., Figures 7e and 10c). More specifically, we show that it is possible (and recommended) to use the smallest window applicable (i.e., two seismic traces) to obtain the finest resolution possible with the available sampling in the upper few meters. The width of the Gaussian functions is also critical because it controls the relative influence of each window with regard to the sampled portion of the subsurface. On the one hand, it has to be wide enough to prevent gaps between windows that would lead to significant information loss at the corresponding wavelengths. However, it also has to be small enough to ensure that all windows are used to describe independent portions of the studied medium and prevent from oversmoothing the retrieved lateral variations. Our parametric study also helped us to determine an optimal Gaussian width, defined with $a = 3$. Along with the resolution, the implementation of MW-WSSW also helps optimizing the lateral extent of the estimated V_S profiles, with an increase of approximately 20% in the case of the Plœmeur data set (i.e., 400–480 m).

In the synthetic and real cases, we used dispersion data at frequencies lower than 10 Hz to provide information at large wavelengths. These frequencies are either damped by the Butterworth filter in the synthetic case or by geophone and source characteristics in the real case. Extracting dispersion information of less than 10 Hz can thus lead to a biased estimation of surface-wave amplitudes and complicate the identification of dispersion curves. Moreover, we chose to use wavelengths larger than the maximum window aperture to enhance the reconstruction of the deeper parts of the velocity model. By doing so, we add information that is not correctly sampled and will likely lead to underestimated phase velocities. This is, however, taken into account when inverting the data by attributing larger error bars at these large wavelengths, and it thus still contributes to characterizing background velocity variations at depth. With previous stacking and windowing techniques, the overall smoothness of the model would be similar at all depths and controlled mainly by the width of the extracting window. Uniform MW-SSW enhances the DOI, but it fails at reproducing short-wavelength lateral variations. With MW-WSSW, we allow for an optimized resolution that decreases with depth, transitioning from a fine characterization of V_S close to the surface to a gross estimation of background velocity at depth. On average, we were able to improve the DOI by 10% in the synthetic case and by 20% in the real case, comparing MW-WSSW with a standard 20 m window. We believe that MW-WSSW provides a better improvement of the DOI in the real case because there is more added value to use MW-WSSW with noisy data than on synthetic/perfect data. Synthetic data are easier to pick at lower frequencies than real data, so the improvement is more pronounced with field data. This improvement allowed us to highlight high-velocity structures hidden with standard stacking procedures. Despite this increase of DOI, structures at depth below 10 m tend to be blurred by the averaging nature of large extracting windows. Furthermore, the limited frequency content of the source (i.e., hammer and plate) prevents retrieving information at depths lower than 25 m, but other sources offering lower frequency content (e.g., accelerated weight drop, vibrator), coupled with lower frequency geophones (i.e., 4 Hz), could be used to make the most of MW-WSSW and infer deeper velocities. Similarly, MW-WSSW could be used to remove signal content that may not be of interest or may be too noisy and, conversely, to boost desirable or higher quality content (e.g., large wavelengths if only targeting deep features).

CONCLUSION

We propose a novel method to estimate 2D lateral variations of subsurface S-wave velocities (V_S) from surface-wave data acquired with typical linear seismic arrays. MW-WSSW is implemented within the open-source SWIP package and is destined to improve dispersion curve extraction along a seismic profile in highly laterally heterogeneous media. In SWIP, local dispersion curves are classically retrieved from stacked dispersion images, which are computed along the seismic profile from successive data subsets extracted within a spatial window spanning the entire data set. The lateral resolution and DOI are then linked to the window aperture used to compute dispersion images. MW-WSSW aims at improving the implemented windowing and stacking methodology to enhance the reconstruction of V_S lateral variations and increase the DOI. MW-WSSW extracts seismic data subsets with multisized windows to compute dispersion images that only characterize specific and reduced ranges of wavelengths (and thus depths) at a single location along the array. By using a set of Gaussian functions, we then weight these dispersion images according to their associated wavelength so that the end result is a final stacked dispersion image in which the amplitudes observed at different frequencies and phase velocities are bound to different portions of the subsurface.

We first performed a parametric study with a simple three-layer model to define optimal parameters for MW-WSSW. We then compared MW-WSSW with standard single-window and uniform (nonweighted) multiwindow stacking on synthetic but more realistic data, and then we applied it to real seismic data obtained at the Plœmeur hydrological observatory. Our results show that MW-WSSW substantially improves the lateral resolution at depths lower than 10 m, with an optimized resolution that decreases with depth while still permitting the depiction of subsurface features down to approximately 25 m. Using MW-WSSW also increases the DOI by 20% and expands the lateral extent of the retrieved profile by approximately 20%. However, the averaging nature of large windows used to characterize deep features still prevents accurately imaging sharp lateral structures at depths lower than 10 m. Moreover, the DOI remains limited by the poor frequency content of the hammer-plate source below 10 Hz, thus preventing us from reaching depths lower than 25 m. Yet this limitation could be overcome by using seismic sources spanning lower frequencies. MW-WSSW is readily implemented in SWIP, and it can now be applied to Rayleigh and Love-

Downloaded 02/18/21 to 194.254.220.11. Redistribution subject to SEG license or copyright; see Terms of Use at https://library.seg.org/page/policies/terms
DOI:10.1190/geo2020-0096.1

wave data for a wide variety of near-surface characterization studies.

ACKNOWLEDGMENTS

The authors would like to thank the two anonymous reviewers, along with the editor-in-chief J. Shragge and associate editor G. Tsoflias, for their constructive and incisive comments that considerably helped improve the paper. We also thank L. Bodet and W. S. Holbrook for their support and valuable discussions throughout the development of MW-WSSW. Acknowledgments are due to L. Longuevergne, the H+ network, and the OZCAR-RI for granting us access to the Plœmeur hydrological observatory. This work was supported by the CRITEX ANR-11-EQPX-0011 project and the Wyoming Experimental Program to Stimulate Competitive Research and National Science Foundation under award EPS-1208909. SWIP and the implemented MW-WSSW are available at https://github.com/SWIPdev/SWIP. The Plœmeur data set (seismic and resistivity) is available in the H+ database (http://hplus.ore.fr/en/ploemeur/data-ploemeur). Synthetic data are available from the first author upon request.

DATA AND MATERIALS AVAILABILITY

Data associated with this research are available and can be obtained by contacting the corresponding author.

REFERENCES

Bergamo, P., D. Boiero, and L. V. Socco, 2012, Retrieving 2D structures from surface-wave data by means of space-varying spatial windowing: Geophysics, **77**, no. 4, EN39–EN51, doi: 10.1190/geo2012-0031.1.

Bergamo, P., B. Dashwood, S. Uhlemann, R. Swift, J. E. Chambers, D. A. Gunn, and S. Donohue, 2016, Time-Lapse monitoring of fluid-induced geophysical property variations within an unstable earthwork using P-wave refraction: Geophysics, **81**, no. 4, EN17–EN27, doi: 10.1190/geo2015-0276.1.

Bodet, L., O. Abraham, and D. Clorennec, 2009, Near-offset effects on Rayleigh-wave dispersion measurements: Physical modeling: Journal of Applied Geophysics, **68**, 95–103, doi: 10.1016/j.jappgeo.2009.02.012.

Bodet, L., K. van Wijk, A. Bitri, O. Abraham, P. Côte, G. Grandjean, and D. Leparoux, 2005, Surface-wave inversion limitations from laser-Doppler physical modeling: Journal of Environmental and Engineering Geophysics, **10**, 151–162, doi: 10.2113/JEEG10.2.151.

Bohlen, T., S. Kugler, G. Klein, and F. Theilen, 2004, 1.5D inversion of lateral variation of Scholte-wave dispersion: Geophysics, **69**, 330–344, doi: 10.1190/1.1707052.

Boiero, D., and L. V. Socco, 2011, The meaning of surface wave dispersion curves in weakly laterally varying structures: Near Surface Geophysics, **9**, 561–570, doi: 10.3997/1873-0604.2011042.

Cardarelli, E., M. Cercato, and G. De Donno, 2014, Characterization of an earth-filled dam through the combined use of electrical resistivity tomography, P- and SH-wave seismic tomography and surface wave data: Journal of Applied Geophysics, **106**, 87–95, doi: 10.1016/j.jappgeo.2014.04.007.

Cheng, F., J. Xia, M. Behm, Y. Hu, and J. Pang, 2019, Automated data selection in the Tau-P domain: Application to passive surface wave imaging: Surveys in Geophysics, **40**, 1211–1228, doi: 10.1007/s10712-019-09530-2.

Dangeard, M., L. Bodet, S. Pasquet, J. Thiesson, R. Guérin, D. Jougnot, and L. Longuevergne, 2018, Estimating picking errors in near-surface seismic data to enable their time-lapse interpretation of hydrosystems: Near Surface Geophysics, **16**, 613–625, doi: 10.1002/nsg.12019.

Di Fiore, V., G. Cavuoto, D. Tarallo, M. Punzo, and L. Evangelista, 2016, Multichannel analysis of surface waves and down-hole tests in the archeological "Palatine Hill" area (Rome, Italy): Evaluation and influence of 2D effects on the shear wave velocity: Surveys in Geophysics, **37**, 625–642, doi: 10.1007/s10712-015-9350-2.

Dumbser, M., and M. Käser, 2006, An arbitrary high-order discontinuous Galerkin method for elastic waves on unstructured meshes — Part 2: The three-dimensional isotropic case: Geophysical Journal International, **167**, 319–336, doi: 10.1111/j.1365-246X.2006.03120.x.

Dumbser, M., M. Käser, and E. F. Toro, 2007, An arbitrary high-order discontinuous Galerkin method for elastic waves on unstructured meshes — Part 5: Local time stepping and p-adaptivity: Geophysical Journal International, **171**, 695–717, doi: 10.1111/j.1365-246X.2007.03427.x.

Dunkin, J. W., 1965, Computation of modal solutions in layered, elastic media at high frequencies: Bulletin of the Seismological Society of America, **55**, 335–358.

Flinchum, B. A., W. S. Holbrook, D. Rempe, S. Moon, C. S. Riebe, B. J. Carr, J. L. Hayes, J. S. Clair, and M. P. Peters, 2018, Critical zone structure under a granite ridge inferred from drilling and three-dimensional seismic refraction data: Journal of Geophysical Research, Earth Surface, **123**, 1317–1343, doi: 10.1029/2017JF004280.

Forbriger, T., 2003, Inversion of shallow-seismic wavefields — Part 1: Wavefield transformation: Geophysical Journal International, **153**, 719–734, doi: 10.1046/j.1365-246X.2003.01929.x.

Gabriels, P., R. Snieder, and G. Nolet, 1987, In situ measurements of shear-wave velocity in sediments with higher-mode Rayleigh waves: Geophysical Prospecting, **35**, 187–196, doi: 10.1111/j.1365-2478.1987.tb00812.x.

Garofalo, F., S. Foti, F. Hollender, P. Y. Bard, C. Cornou, B. R. Cox, M. Ohrnberger, D. Sicilia, M. Asten, G. Di Giulio, T. Forbriger, B. Guillier, K. Hayashi, A. Martin, S. Matsushima, D. Mercerat, V. Poggi, and H. Yamanaka, 2016, InterPACIFIC project: Comparison of invasive and non-invasive methods for seismic site characterization — Part 1: Intra-comparison of surface wave methods: Soil Dynamics and Earthquake Engineering, **82**, 222–240, doi: 10.1016/j.soildyn.2015.12.010.

Grandjean, G., and A. Bitri, 2006, 2M-SASW: Multifold multichannel seismic inversion of local dispersion of Rayleigh waves in laterally heterogeneous subsurfaces: Application to the Super-Sauze earthflow, France: Near Surface Geophysics, **4**, 367–375, doi: 10.3997/1873-0604.2006010.

Groos, L., M. Schäfer, T. Forbriger, and T. Bohlen, 2017, Application of a complete workflow for 2D elastic full-waveform inversion to recorded shallow-seismic Rayleigh waves: Geophysics, **82**, no. 2, R109–R117, doi: 10.1190/geo2016-0284.1.

Haskell, N. A., 1953, The dispersion of surface waves on multilayered media: Bulletin of the Seismological Society of America, **43**, 17–34, doi: 10.1029/SP030p0086.

Herrmann, R. B., 2013, Computer programs in seismology: An evolving tool for instruction and research: Seismological Research Letters, **84**, 1081–1088, doi: 10.1785/0220110096.

Ikeda, T., T. Matsuoka, T. Tsuji, and T. Nakayama, 2015, Characteristics of the horizontal component of Rayleigh waves in multimode analysis of surface waves: Geophysics, **80**, no. 1, EN1–EN11, doi: 10.1190/geo2014-0018.1.

Ikeda, T., T. Tsuji, and T. Matsuoka, 2013, Window-controlled CMP cross-correlation analysis for surface waves in laterally heterogeneous media: Geophysics, **78**, no. 6, EN95–EN105, doi: 10.1190/geo2013-0010.1.

Jaganathan, A. P., 2019, Multichannel surface wave analysis of reinforced concrete pipe segments using longitudinal and circumferential waves induced by a point impact: Journal of Applied Geophysics, **163**, 40–54, doi: 10.1016/j.jappgeo.2019.02.010.

Käser, M., and M. Dumbser, 2006, An arbitrary high-order discontinuous Galerkin method for elastic waves on unstructured meshes — Part 1: The two-dimensional isotropic case with external source terms: Geophysical Journal International, **166**, 855–877, doi: 10.1111/j.1365-246X.2006.03051.x.

Käser, M., and M. Dumbser, 2008, A highly accurate discontinuous Galerkin method for complex interfaces between solids and moving fluids: Geophysics, **73**, no. 3, T23–T35, doi: 10.1190/1.2870081.

Käser, M., P. M. Mai, and M. Dumbser, 2007, Accurate calculation of fault-rupture models using the high-order discontinuous Galerkin method on tetrahedral meshes: Bulletin of the Seismological Society of America, **97**, 1570–1586, doi: 10.1785/0120060253.

Keifer, I., K. Dueker, and P. Chen, 2019, Ambient Rayleigh wave field imaging of the critical zone in a weathered granite terrane: Earth and Planetary Science Letters, **510**, 198–208, doi: 10.1016/j.epsl.2019.01.015.

Kennett, B. L. N., 1974, Reflections, rays, and reverberations: Bulletin of the Seismological Society of America, **64**, 1685–1696.

Khosro Anjom, F., D. Teodor, C. Comina, R. Brossier, J. Virieux, and L. V. Socco, 2019, Full-waveform matching of VP and VS models from surface waves: Geophysical Journal International, **218**, 1873–1891, doi: 10.1093/gji/ggz279.

Lai, C. G., G. J. Rix, S. Foti, and V. Roma, 2002, Simultaneous measurement and inversion of surface wave dispersion and attenuation curves: Soil Dynamics and Earthquake Engineering, **22**, 923–930, doi: 10.1016/S0267-7261(02)00116-1.

Lu, Z., G. V. Wilson, and M. W. Shankle, 2019, Measurements of soil profiles in the vadose zone using the high-frequency surface waves method: Journal of Applied Geophysics, **169**, 142–153, doi: 10.1016/j.jappgeo.2019.07.002.

McMechan, G. A., and M. J. Yedlin, 1981, Analysis of dispersive waves by wave field transformation: Geophysics, **46**, 869–874, doi: 10.1190/1.1441225.

Downloaded 02/18/21 to 194.254.220.11. Redistribution subject to SEG license or copyright; see Terms of Use at https://library.seg.org/page/policies/terms
DOI:10.1190/geo2020-0096.1

Mi, B., J. Xia, J. H. Bradford, and C. Shen, 2020, Estimating near-surface shear-wave-velocity structures via multichannel analysis of Rayleigh and love waves: An experiment at the Boise hydrogeophysical research site: Surveys in Geophysics, **41**, 323–341, doi: 10.1007/s10712-019-09582-4.

Mi, B., J. Xia, C. Shen, and L. Wang, 2018, Dispersion energy analysis of Rayleigh and love waves in the presence of low-velocity layers in near-surface seismic surveys: Surveys in Geophysics, **39**, 271–288, doi: 10.1007/s10712-017-9440-4.

Mi, B., J. Xia, C. Shen, L. Wang, Y. Hu, and F. Cheng, 2017, Horizontal resolution of multichannel analysis of surface waves: Geophysics, **82**, no. 3, EN51–EN66, doi: 10.1190/geo2016-0202.1.

Mokhtar, T. A., R. B. Herrmann, and D. R. Russell, 1988, Seismic velocity and Q model for the shallow structure of the Arabian Shield from short-period Rayleigh waves: Geophysics, **53**, 1379–1387, doi: 10.1190/1.1442417.

Naskar, T., and J. Kumar, 2019, A faster scheme to generate multimodal dispersion plots for Rayleigh wave propagation: Soil Dynamics and Earthquake Engineering, **117**, 280–287, doi: 10.1016/j.soildyn.2018.11.024.

Neducza, B., 2007, Stacking of surface waves: Geophysics, **72**, no. 2, V51–V58, doi: 10.1190/1.2431635.

Olafsdottir, E. A., B. Bessason, and S. Erlingsson, 2018, Combination of dispersion curves from MASW measurements: Soil Dynamics and Earthquake Engineering, **113**, 473–487, doi: 10.1016/j.soildyn.2018.05.025.

O'Neill, A., 2003, Full-waveform reflectivity for modelling, inversion and appraisal of seismic surface wave dispersion in shallow site investigations: Ph.D. thesis, University of Western Australia, Perth, Australia.

O'Neill, A., M. Dentith, and R. List, 2003, Full-waveform P-SV reflectivity inversion of surface waves for shallow engineering applications: Exploration Geophysics, **34**, 158–173, doi: 10.1071/EG03158.

Onnis, L. E., A. Osella, and J. M. Carcione, 2019, Retrieving shallow shear-wave velocity profiles from 2D seismic-reflection data with severely aliased surface waves: Journal of Applied Geophysics, **161**, 15–25, doi: 10.1016/j.jappgeo.2018.11.014.

Pan, Y., L. Gao, and T. Bohlen, 2019, High-resolution characterization of near-surface structures by surface-wave inversions: From dispersion curve to full waveform: Surveys in Geophysics, **40**, 167–195, doi: 10.1007/s10712-019-09508-0.

Park, C. B., R. D. Miller, and J. Xia, 1999, Multichannel analysis of surface waves: Geophysics, **64**, 800–808, doi: 10.1190/1.1444590.

Pasquet, S., and L. Bodet, 2017, SWIP: An integrated workflow for surface-wave dispersion inversion and profiling: Geophysics, **82**, no. 6, WB47–WB61, doi: 10.1190/geo2016-0625.1.

Pasquet, S., L. Bodet, P. Bergamo, R. Guérin, R. Martin, R. Mourgues, and V. Tournat, 2016a, Small-scale seismic monitoring of varying water levels in granular media: Vadose Zone Journal, **15**, 1–14, doi: 10.2136/vzj2015.11.0142.

Pasquet, S., L. Bodet, A. Dhemaied, A. Mouhri, Q. Vitale, F. Rejiba, N. Flipo, and R. Guérin, 2015a, Detecting different water table levels in a shallow aquifer with combined P-, surface and SH-wave surveys: Insights from VP/VS or Poisson's ratios: Journal of Applied Geophysics, **113**, 38–50, doi: 10.1016/j.jappgeo.2014.12.005.

Pasquet, S., L. Bodet, L. Longuevergne, A. Dhemaied, C. Camerlynck, F. Rejiba, and R. Guérin, 2015b, 2D characterization of near-surface VP/VS: Surface-wave dispersion inversion versus refraction tomography: Near Surface Geophysics, **13**, 315–332, doi: 10.3997/1873-0604.2015028.

Pasquet, S., W. S. Holbrook, B. J. Carr, and K. W. W. Sims, 2016b, Geophysical imaging of shallow degassing in a Yellowstone hydrothermal system: Geophysical Research Letters, **43**, 12,027, doi: 10.1002/2016GL071306.

Pegah, E., and H. Liu, 2016, Application of near-surface seismic refraction tomography and multichannel analysis of surface waves for geotechnical site characterizations: A case study: Engineering Geology, **208**, 100–113, doi: 10.1016/j.enggeo.2016.04.021.

Petronio, L., J. Boaga, and G. Cassiani, 2016, Characterization of the Vajont landslide (North-Eastern Italy) by means of reflection and surface wave seismics: Journal of Applied Geophysics, **128**, 58–67, doi: 10.1016/j.jappgeo.2016.03.012.

Ruelleu, S., F. Moreau, O. Bour, D. Gapais, and G. Martelet, 2010, Impact of gently dipping discontinuities on basement aquifer recharge: An example from Plœmeur (Brittany, France): Journal of Applied Geophysics, **70**, 161–168, doi: 10.1016/j.jappgeo.2009.12.007.

Russel, D. R., 1987, Multi-channel processing of dispersed surface waves: Ph.D. thesis, Saint Louis University, Saint Louis, Missouri, USA.

Sambridge, M., 1999, Geophysical inversion with a neighbourhood algorithm — Part 2: Appraising the ensemble: Geophysical Journal International, **138**, 727–746, doi: 10.1046/j.1365-246x.1999.00900.x.

Serdyukov, A. S., A. V. Yablokov, A. A. Duchkov, A. A. Azarov, and V. D. Baranov, 2018, Slant f-k transform of multichannel seismic surface wave data: Geophysics, **84**, no. 1, A19–A24, doi: 10.1190/geo2018-0430.1.

Shakas, A., N. Linde, L. Baron, O. Bochet, O. Bour, and T. L. Borgne, 2016, Hydrogeophysical characterization of transport processes in fractured rock by combining push-pull and singlehole ground penetrating radar experiments: Water Resources Research, **52**, 938–953, doi: 10.1002/2015WR017837.

Socco, L. V., and D. Boiero, 2008, Improved Monte Carlo inversion of surface wave data: Geophysical Prospecting, **56**, 357–371, doi: 10.1111/j.1365-2478.2007.00678.x.

Socco, L. V., S. Foti, and D. Boiero, 2010, Surface-wave analysis for building near-surface velocity models — Established approaches and new perspectives: Geophysics, **75**, no. 5, 75A83–75A102, doi: 10.1190/1.3479491.

Socco, L. V., and C. Strobbia, 2004, Surface-wave method for near-surface characterization: A tutorial: Near Surface Geophysics, **2**, 165–185, doi: 10.3997/1873-0604.2004015.

Strobbia, C., and S. Foti, 2006, Multi-offset phase analysis of surface wave data (MOPA): Journal of Applied Geophysics, **59**, 300–313, doi: 10.1016/j.jappgeo.2005.10.009.

Thomson, W. T., 1950, Transmission of elastic waves through a stratified solid medium: Journal of Applied Physics, **21**, 89–93, doi: 10.1063/1.1699629.

Wang, W., P. Chen, I. Keifer, K. Dueker, E.-J. Lee, D. Mu, J. Jiao, Y. Zhang, and B. Carr, 2019a, Weathering front under a granite ridge revealed through full-3D seismic ambient-noise tomography: Earth and Planetary Science Letters, **509**, 66–77, doi: 10.1016/j.epsl.2018.12.038.

Wang, W., P. Chen, E.-J. Lee, and D. Mu, 2019b, Full-3D seismic tomography for structure of the critical zone, in earthquake and disaster risk: Decade retrospective of the Wenchuan Earthquake: Springer, 203–231.

Wathelet, M., 2008, An improved neighborhood algorithm: Parameter conditions and dynamic scaling: Geophysical Research Letters, **35**, L09301, doi: 10.1029/2008GL033256.

Wathelet, M., D. Jongmans, and M. Ohrnberger, 2004, Surface-wave inversion using a direct search algorithm and its application to ambient vibration measurements: Near Surface Geophysics, **2**, 211–221, doi: 10.3997/1873-0604.2004018.

Xia, J., Y. Xu, Y. Luo, R. D. Miller, R. Cakir, and C. Zeng, 2012, Advantages of using multichannel analysis of love waves (MALW) to estimate near-surface shear-wave velocity: Surveys in Geophysics, **33**, 841–860, doi: 10.1007/s10712-012-9174-2.

Biographies and photographs of the authors are not available.